RESEARCH ON TRANSONIC WINGS AT THE NATIONAL AEROSPACE LABORATORY, JAPAN

Nobuhiko Kamiya and Naoki Hirose
National Aerospace Laboratory
Tokyo, Japan

Abstract

A brief review is made of the recent research on transonic wings being conducted at the NAL in Japan with the aim of improving transonic performance of aircraft. It consists of two parts. One is the research on transonic aerodynamics and the other is the research on the optimization of transonic wings using such aerodynamics as a tool.

Firstly, research on aerodynamics is described, which includes design of shock free airfoils using the hodograph method; numerical design of shock free airfoils using the method of artificial gas; numerical design of airfoils with a shock wave by use of the relaxation method; two kinds of numerical analyses of unsteady flow around airfoils, one using Euler equations and the other using full potential equations; and analysis of flow around three dimensional wings by use of integral equations. Some remarks are also made about the viscous effect evaluation.

Secondly, research on optimization of transonic airfoils is described. The evaluation of the airfoil analysis code is also described.

Finally, a brief review is made of two kinds of facilities; one is the two-dimensional high Reynolds number wind tunnel, and the other is our numerical simulation project.

I. Introduction

Significant improvements in fuel efficiency has been established through the application of supercritical aerodynamics to wing design. However, most of the advanced technology wings currently in use have been designed not by the transonic flow theory but by use of empirical knowledge about the relationships between the pressure distributions in transonic flow and those in fully subsonic flow, or the curvature distribution of wing surfaces, due to the lack in adequate theory for transonic flow.

NAL has developed a series of airfoils[1, 2], also by use of the theory for fully subsonic flow. A significant progress in computational aerodynamics during the 1970's, however, has made it possible to design wings using transonic flow theory. It has become necessary to establish a methodology for designing optimum wings using transonic flow theory.

Another defect, concerning the advanced technology wings in current use, is that the values of the Reynolds number, tested in wind tunnels, have been too low compared with those experienced in prectical flight. It has been recognized [3] that the aerodynamic characteristics of wings at transonic speeds are sometimes significantly different, depending on the values of the Reynolds number tested, due to the difference in the behavior of the shock boundary layer interaction. In order to overcome this deficiency, several wind tunnels, for high Reynolds number tests, have been constructed [4, 5] and one is now being constructed [6], a two dimensional pressure wind tunnel has been constructed at NAL [5] and the intial calibration of it has just begun.

NAL has a plan to establish a design methodology of advanced technology wings by use of two kinds of tools mentioned above, computational aerodynamics and a high Reynolds number wind tunnel. In the present paper what has been conducted so far at NAL, concerning this plan, is described.

II. Hodograph Method

Shigemi[7] developed a method of designing shock free airfoils based on the analytical hodograph method. The solutions of hodograph equations for the transonic flow around airfoils have been obtained [8, 9] by a transformation of the known solution of incompressible flow to that of the transonic flow. Shigemi called the incompressible flow, which marks the starting point of this transformation, as a "model" flow.

What he was mostly concerned with was the "model" problem. From the viewpoint of the practical design problem of lifting transonic airfoil sections, two kinds of models have been used; one is the lifting elliptic cylinder model [8] and the other is the combined model of a lifting circular cylinder and a non-lifting elliptic cylinder [9]. As to the former, one is inclined to consider its use rather prohibitive, due primarily to the complexities involved in theory and in numerical computation, and also due to difficulties experienced in producing cambered sections. As to the latter, however, it is difficult to produce sections having a large angle of attack with the free stream.

But there is still another possibility: Shigemi introduced a new model, tentatively named "YC-profile", as an improvement on existing models. It is originated from the attempt to compose a hodograph of a lifting wing-like body with mathematical expression as simple as possible.

Fig. 1 (a) shows the streamlines of an incompressible flow around a lifting circular cylinder in the physical plane. Fig. 1 (b) shows those in the hodograph ζ-plane where $\zeta = qe^{i\theta}$, q and θ are the magnitude and the angular direction, respectively, of the local velocity. It can be seen that flow is defined on the two sheeted Rieman surface in ζ-plane where ζ_B denotes the branch point. If ζ is transformed to ξ by

$$\xi = (1-\zeta/\zeta_B)^{1/2}, \qquad (1)$$

then $\zeta = \zeta_B$ is mapped onto the origin of ξ-plane as shown in Fig. 1 (c), whereas the point $\zeta_U(=1)$, corresponding to the uniform flow, is mapped on to the point $\xi_U = (1-1/\zeta_U)^{1/2}$. In this case the effective flow occupying the outside of the circle $|z| = 1$ in z-plane is now mapped inside of a circle defined by $|\xi-\xi_U| = 1/\sqrt{1-k^2}$ in ξ-plane.

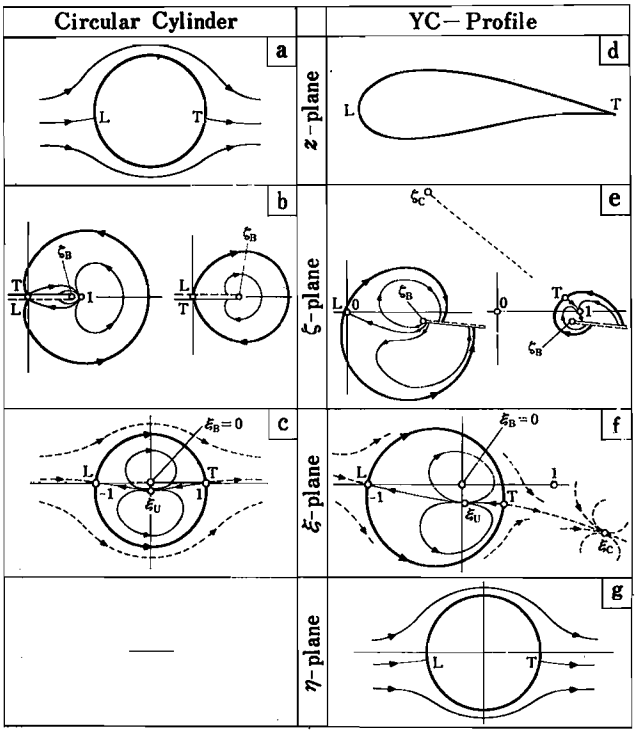

Fig. 1. Comparison of incompressible flows in physical(z), hodograph(ζ), and regularized hodograph(ξ) planes.

The center of this circle is located at $\xi = \xi_U$, where the complex velocity potential w exhibits its singularity comprising a dipole and a vortex.

Consider a more general case where the dipole-and-vortex singularity (the location of which is denoted throughout by ξ_U) lies apart from the center of a circle; the circle is now arbitrary, but assumed to constitute ultimately the streamline $\Psi = 0$ of the hypothetical flow. In this respect, the genesis of YC-profiles is somewhat like that of Joukowski profiles; and in fact they are expected to play a role similar to that which Joukowski profiles once played in classical wing theory.

If we introduce another transformation

$$\eta = \eta_R \frac{\xi-\xi_C}{\xi-\xi_U} \left(= \eta_R - ik \frac{1-\xi_U^2}{\xi_U} \frac{1}{\xi-\xi_U} \right), \qquad (2)$$

where

$$\eta_R = \frac{ik(1-\xi_U^2)}{\xi_U(\xi_C-\xi_U)} \qquad (3)$$

denotes the value of η corresponding to $\xi = \infty$, the geometry of the streamlines in η-plane shown in Fig. 1 (g) is exactly the same as that in z-plane shown in Fig. 1 (a).

The image in z-plane of the unit circle $|\eta| = 1$ in η-plane, which will tentatively be called YC-profile, takes a shape with a round nose and a cusped tail, and is somewhat like a Joukowski profile (see Fig. 1,d). In Fig. 2 are shown a series of YC-profiles with fixed γ and varied parameters $|\eta_R|$ and $\arg.\eta_R$.

The complex velocity potential of the YC-profile, in terms of the hodograph variables, is substantially similar to that for a circular

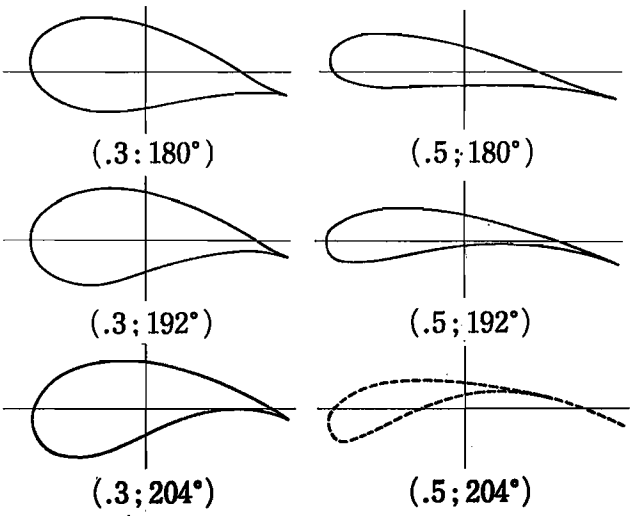

Fig. 2. YC-profiles
Parameters: γ = 12° (fixed), $[|\eta|, \arg.\eta]$.

cylinder and quite easy to handle in the hodograph theory. Nevertheless, the shape of a YC-profile in the physical plane, which happens to be somwwhat like a Joukowski profile, satisfies the minimum requirements -- including varied thickness, camber and angle of attack -- for practical wing sections.

One drawback in the analytical hodograph method is that, even if the model be given as a normal flow around a closed body, the transformed contour for the compressible flow might not close at the trailing edge. It is possible to close the trailing edge by superposing an adequate solution of the fundamental hodograph equation. In Fig. 3 a typical supercritical airfoil section based on a YC profile is shown.

Superposition of a few more arbitrary solutions to the basic function of a YC-profile is useful in order to design wing sections of a wider scope. Fig. 4 shows the example of airfoils transformed from YC-profiles modified in such a way.

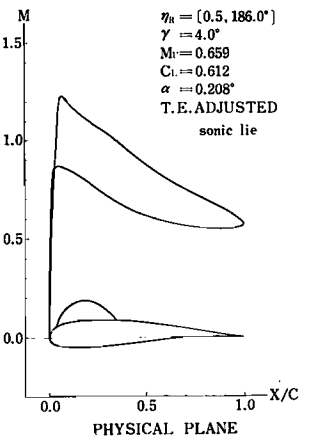

Fig. 3. A transonic YC-profile (YC-0054)

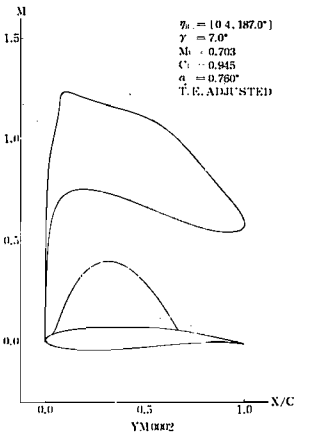

Fig. 4. A modified transonic YC-profile (YM-0002).

III. Computational Aerodynamics

1. Transonic Airfoil Design

(1) Method of Artificial Gas

Nakamura (10, 11, 12) developed a new method of designing shock free airfoils based, not on the hodograph method, but on analysis in the physical plane, which is similar to the method of Ref. (13) He adopted the following equation as a fundamental equation of two dimensional isentropic flow

$$\frac{\partial^2\Psi}{\partial x^2} + \frac{\partial^2\Psi}{\partial y^2} + \frac{\partial M^2/\partial x}{2+(\gamma-1)M^2} \cdot \frac{\partial\Psi}{\partial x} + \frac{\partial M^2/\partial y}{2+(\gamma-1)M^2} \cdot \frac{\partial\Psi}{\partial y} = 0 \qquad (4)$$

where Ψ is stream function, γ is the ratio of the specific heat and M is a local Mach number which is related with Ψ by the following equation.

$$\left\{\left(\frac{\partial\Psi}{\partial x}\right)^2 + \left(\frac{\partial\Psi}{\partial y}\right)^2\right\} / (a_0\rho_0)^2 = f(M) \qquad (5)$$

where a_0 and ρ_0 are speed of sound and density at stagnation point respectively and f(M) is defined by

$$f(M) = M^2\left(1 + \frac{\gamma-1}{2} M^2\right)^{-\frac{\gamma+1}{\gamma-1}} \qquad (6)$$

Eq. (4) is of the elliptic type in the subsonic region where $\frac{df}{dM} > 0$ and of the hyperbolic type in the supersonic region where $\frac{df}{dM} < 0$. Nakamura temporary replaced f(M) of Eq. (5) by g(M), giving,

$$\left\{\left(\frac{\partial\Psi}{\partial x}\right)^2 + \left(\frac{\partial\Psi}{\partial y}\right)^2\right\} / (a_0\rho_0)^2 = g(M) \qquad (5')$$

where g(M) is a smooth function of M which satisfies

$$g(M) = f(M) \quad \text{at } M \leqq 1$$
$$\frac{dg(M)}{dM} > 0 \quad \text{at } M > 1 \qquad (7)$$

If M is related with Ψ by Eq. (5'), then Eq. (4) turns out to be of the elliptic type everywhere exept on the sonic line. Eq. (4) supplemented by Eq. (5') is a differential equation of the flow of an artificial gas, which is different from the real gas only in the supersonic region and exactly the same as the real gas in the subsonic region. This gas is hereby reffered to as Nakamura's gas. In the case of the accelerating flow of Nakamura's gas in ducts, the cross sectional area decreases monotonically both in the subsonic and supersonic region in contrast to the case of the real gas where the cross sectional area decreases in the subsonic region and increases in the supersonic region.

High subsonic flows of Nakamura's gas around an arbitrary airfoil can easily be solved by the relaxation method, yielding a local supersonic region (region P in Fig. 5). The supersonic part of the solution does not represent the flow of real gas whereas the subsonic part represents the flow of real gas exactly.

If one solves the initial value problem of Eqs. (4) and (5) in the region P using data at the sonic line as initial values, by the method of characteristics, for example, then one obtains a continuous supersonic flow of real gas if the choice of a free stream Mach number and the function g(M) is apropriate.

Fig. 6 shows an example of the mesh of characteristics. The stream line AB'C, obtained from the solution, produces a new shock free airfoil geometry partially modified from the original airfoils.

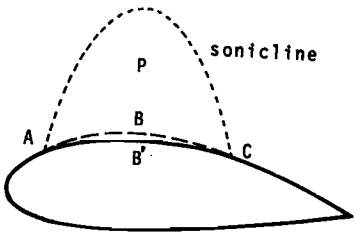

Fig. 5. Original and modified airfoils.

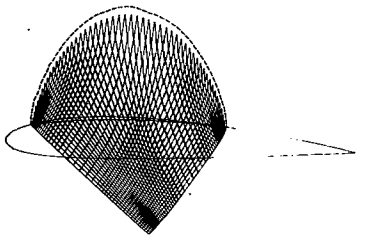

Fig. 6. Mesh of characteristics.

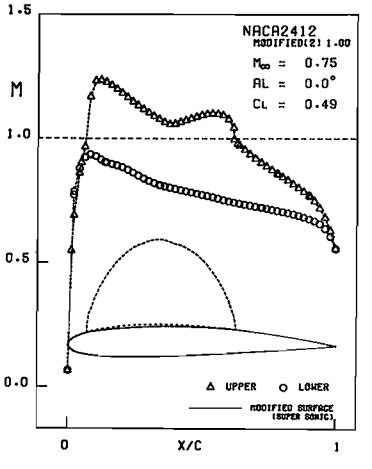

Fig. 7. An airfoil modified from NACA2412.

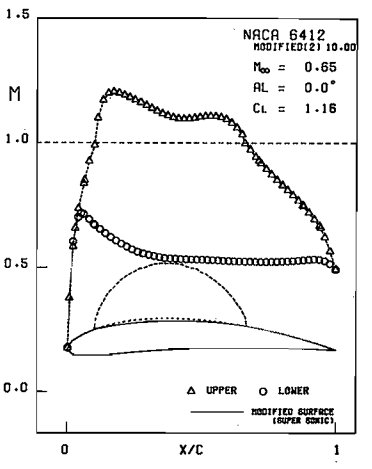

Fig. 8. An airfoil modified from NACA6412.

As stream tube of Nakamura's gas is narrower than that of real gas, in the supersonic region, the new airfoil is necessarily thinner than the original one. If the choice of the free stream Mach number or the function g(M) are not appropriate, a limit line appears in the solution, and continuous shock free solution fails to be obtained. The function g(M) for M > 1, in his calculation, is chosen as follows.

$$g(M) = \left(\frac{\gamma+1}{2}\right)^{-\frac{\gamma+1}{\gamma-1}} + A(M^2-1)^2 \quad (M > 1) \qquad (8)$$

where A is a positive real constant.

Some examples of the shock free airfoils partially modified from NACA 4 digit airfoils are shown in Figs. 7 and 8.

A special merit of the present method is that the initial airfoil sections can be given arbitrarily and that various airfoil sections can be obtained by the choice of the function g(M).

An additional merit is that this method can be applied to three dimensional wing-body combinations.

(2) Relaxation Method

Ishiguro[14] developed an effective design method for designing a transonic airfoil having specified pressure distributions without regard to the existence of shock waves. The fundamental idea of the method is due to Tranen[15]. The procedure is to repeat the following two steps of transonic full potential relaxation calculations until the solution of the "direct step" give a surface pressure distribution coincident with the specified design pressure distribution. The final "designed" airfoil geometry is obtained by subtracting the displacement thickness of the boundary layer from the final temporary airfoil given as the solution of the "inverse" step.

1. Direct Step: the full potential equation(9),

$$(a^2-U^2)\phi_{xx} - 2UV\phi_{xy} + (a^2-V^2)\phi_{yy} = 0 \qquad (9)$$

is solved for a temporary airfoil geometry given as the Neumann's boundary condition using the type-dependent relaxation method.

2. Inverse Step: the same equation (9) is solved this time as the Dirichlet's boundary problem by specifying the design pressure distribution on the temporary airfoil geometry. The solution obtained does not generally satisfy the zero normal velocity boundary condition on the temporary airfoil surface. An adjustment is made to modify the airfoil geometry so that the boundary condition is satisfied.

In Tranen's method, the man-in-the-loop procedure was necessary and it took about one hour of computing time to solve the problem. In the present method, however, the procedure is completely automated without any man-in-the-loop procedure. The computing time is reduced to only 130 sec on the NAL AP system in batch mode for most reasonably-formed design pressure distributions. The following improvements have been made. The relaxation scheme was changed to the more advanced Jameson's rotated difference scheme, incorporating the Poisson solver[16]. The initial potential distribution to start the relaxation is given from the solution of the previous step so as to satisfy the boundary condition. This reduced a large amount the computing time. The temporary airfoil is rotated to yield the specified lift coefficient C_L. The potential at imaginary boundary grid point inside of airfoil contour is solved simultaneously along with the internal grid points using line relaxation. The boundary layer effect is incorporated by calculating the displacement thickness. The actual airfoil geometry is obtained by subtracting the displacement thickness from the converged temporary airfoil geometry.

The actual computing procedure is given as the following flow chart.

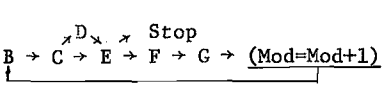

The outline of the each iterative step is described.

A. Input: Design pressure distribution, $C_p(x)$, on the upper and lower surfaces and free stream Mach number, M_∞, are given as the input. The x axis is taken as parallel to the free stream direction. The surface distribution of the local Mach number, M, density, p, velocity, U, and the lift coefficient, C_L, are then obtained from the specified pressure distribution. The initial temporary airfoil geometry is also input arbitrarily. In the program, families of initial airfoils are programmed and one can choose any of them specifying a parameter.

B. Rotation of the temporary airfoil: The angle of attack, $\tilde{\alpha}$, at which the value of C_L of the temporary airfoil is equal to the specified C_L is calculated by the use of the direct method (direct step). The temporary airfoil is rotated to have the angle of attack of $\tilde{\alpha}$. The trailing edge, with finite value of thickness given, is modified to be perpendicular to the x axis.

C. Direct problem of the temporary airfoil: Again the flow past the rotated airfoil is calculated using the direct step now with the angle of attack fixed. The pressure distribution $C_p(x)$ is obtained.

D. Calculation of the displacement thickness of the boundary layer: The turbulent boundary layer and its displacement thickness are calculated from the $C_p(x)$ obtained above by use of the Nash and MacDonald's method. The temporary actual airfoil geometry is obtained by subtracting the displacement thickness from the temporary airfoil geometry.

E. Test on convergence: The criterion of the convergence of design loop is given by the mean weighted square of pressure distribution difference between the specified design distribution and the one obtained in step C. A specified value of the criterion is given as an input. The loop is also stopped by specifying the total computing time or maximum number of iteration loops, Mod.

F. Inverse problem step: The temporary airfoil geometry given at step B is not an inpermeable solid boundary but is assumed to be a contour in the flow field on which the tangential velocity component is specified as U. Here, U is as given previously in step A. The normal velocity component, V_n, is calculated, using the finite difference once the potential distribution has

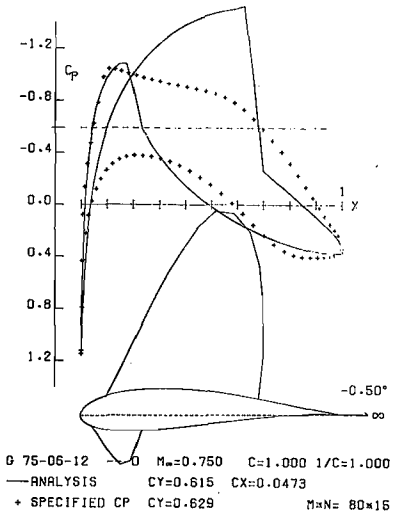

Fig. 9(a)

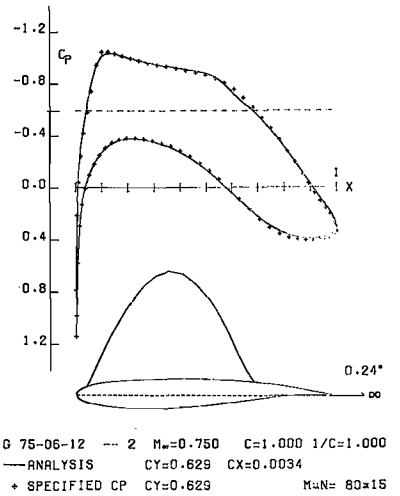

Fig. 9(b)

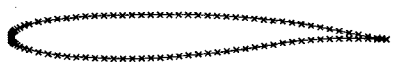

— ORIGINAL × PRESENT METHOD

Fig. 9(c)

Fig. 9. Inviscid shock-free supercritical airfoil design.

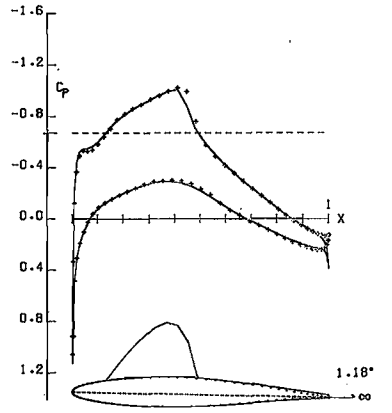

Fig. 10(a)

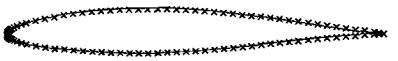

— ORIGINAL × PRESENT METHOD

Fig. 10(b)

Fig. 10. Design for NACA 64_1-212 using experimental data.

been obtained, as the solution. The solution is obtained for specified circulation, Γ, i.e. specified C_L, and closure condition, $C_Q \equiv \oint_C V_n ds = 0$. Jameson's rotated difference scheme with Poisson solver are modified to use in the present inverse problem setting. Conformal mapping into a unit circle, reduced potential form and simultaneous line - relaxation, including an imaginary boundary grid point are used for improving the convergence.

G. Modification of temporary airfoil geometry: The velocity distribution, in the neighborhood of the temporary airfoil geometry, was obtained in the previous step. Normal velocity, V_n, along the geometry does not vanish if the design loop is not convergent. A new contour, on which the normal velocity vanishes, is sought using the mass flow relation between the new contour, that is the new airfoil geometry, and the old temporary airfoil geometry. The design loop goes back to step B now with the new contour as the temporary airfoil geometry.

To confirm the capability of the present design method, one of the inviscid shock-free supercritical airfoils of Garabedian was reproduced. The surface pressure distribution, C_p, for the Garabedian airfoil[17], 75-06-12, was used as the input design distribution. The calculation was made as the inviscid flow case of Mach number, $M_\infty = 0.75$, and lift coefficient, $C_L = 0.629$. The step D was bypassed since there was no boundary layer modification. The scheme used was a nonconservative relaxation scheme in the present and the following cases. The result is shown in Fig. 9.

In Fig. 9(a), the design C_p's are shown by mark +. The solid line represents the obtained C_p distribution for the initial temporary airfoil geometry. A strong shock wave appears on the upper surface. With only two iteration loops, however the converged shock-free airfoil geometry is obtained. The pressure distribution for the converged airfoil geometry is shown in Fig. 9(b) and compared with the design distribution.

The agreement is excellent. The designed airfoil geometry and sonic line are also shown in the same figure. The comparison with the original airfoil geometry designed by Garabedian's Hodograph method is made in Fig. 9(c). The agreement is also excellent.

Next, a viscous flow design, using an experimental data for NACA 64_1-212[2], was tried. The design condition was Mach number, $M_\infty = 0.728$, lift coefficient, $C_L = 0.425$ and Reynolds number, $Re = 2 \times 10^6$. A converged solution was obtained at the iteration loop made of 4. The pressure distribution is shown in Fig. 10(a). The agreement is remarkable except for the shock and the trailing edge regions. At the shock region, the solution is represented by a discrete finite difference solution of finite grid point width while the experimental pressure distribution is smeared due to the shock boundary layer interaction. At the region close to the trailing edge, separation occurs in the experiemnt which cannot be taken into account in the calculation and some kind of means for the extrapolation of C_p is accomodated to obtain the converged numerical solution. A severe convergence criterion at such regions is not neccesarily required. Rather, an appropriate relaxation of criterion by a weighting function leads to a better result. The airfoil geometry shown by the solid line is the contour before the boundary layer thickness is subtracted and has a finite trailing edge width. The small dots represent the final actual geometry which has a closed trailing edge.

In Fig. 10(b), a comparison was made with the original NACA 64_1-212. The overall agreement was obtained as can be seen in the overlapped

plot of contours while a small discrepancy, noticeable in the afterbody region, may be attributed to the insufficient turbulent boundary layer correction.

Further examples of this calculations will be described later in IV. 1.

2. Unsteady Aerodynamics

(1) Small Perturbation Analysis

In the field of unsteady transonic aerodynamics, a computer program based on the two-dimensional transonic small perturbation equation (TSP equation), has been developed by Isogai.[18]

The transonic small perturbation equation expressed by the dimensionless quantities is given by

$$(1-M_\infty^2-(\gamma+1)M_\infty^m\phi_x)\phi_{xx} + \phi_{yy} - 2M_\infty^2\phi_{xt} - M_\infty^2\phi_{tt} = 0 \qquad (10)$$

where M_∞ and ϕ are the freestream Mach number and the perturbation velocity potential, respectively, and a constant m is adjusted to match the critical pressure coefficient C_p^* to its exact isentropic value.[19]. The flow tangency condition is given at y = 0. At the far-field boundaries, the following conditions are satisfied:

$$\phi = \frac{\Gamma^{(s)}}{2\pi}\left\{\frac{\pi}{2}\,\mathrm{sgn}(y) + \tan^{-1}\left(\frac{x}{\beta y}\right)\right\} \quad \text{for } M_\infty < 1 \qquad (11)$$

or

$$\left.\begin{array}{ll} \phi = 0 & \text{upstream of the shock wave} \\ \phi_y = 0 & \text{downstream of the shock wave} \end{array}\right\} \text{for } M_\infty \gtrsim 1 \qquad (12)$$

In Eq. (11), $\Gamma^{(s)}$ is the mean steady-state value of the circulation and β is defined by $\sqrt{1-M_\infty^2}$.

The above boundary value problem was solved numerically, in the stretched Cartesian grid system, by applying a time-marching, semi-implicit and implicit, two sweep procedure. To capture the shock wave motions properly, a quasi-conservative scheme[20-22] was employed.

The present TSP code can be used for the calculations of the unsteady aerodynamic forces in the wide range of the reduced frequency, based on semichord, $0 \lesssim k \lesssim 0.5$, at the transonic Mach numbers from subcritical to above Mach 1. To see the capability of the code, the calculations were performed for a NACA64A010 airfoil oscillating in pitch about quarter-chord axis at Mach number 0.80, for which the experimental data[23,24] are available. In Fig. 11, the mean steady pressure distribution is shown, being compared with the experimental data of Ref. 23.

A relatively weak shock is present near midchord. In Fig. 12, the chordwise distributions of the in-phase and out-of-phase components of the first harmonic of the upper surface pressure, are shown, being compared with the experimental data[23]. The reduced frequency considered is 0.2. The peak value of the in-phase component and the rapid variation of the out-of-phase component observed around midchord are the effects of the shock wave. The agreement of the present finite difference calculations with the experiment is satisfactory.

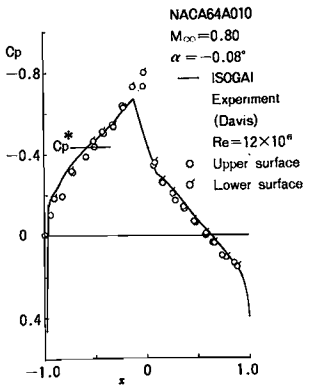

Fig. 11. Steady pressure distribution on NACA 64A010 airfoil.

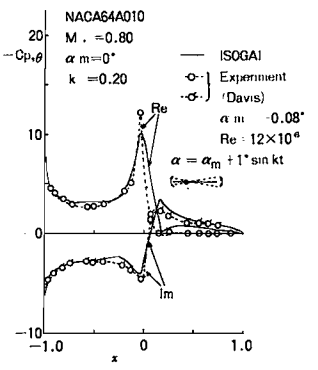

Fig. 12. Upper surface unsteady pressure distribution on NACA64A010 airfoil oscillating in pitch about quarter-chord axis.

In Fig. 13(a) and Fig. 13(b), the variation of the in-phase and out-of-phase components of the first-harmonic of lift and pitching moment (about the leading edge) versus reduced frequency are compared with the experimental data and those predicted by the linear theory (the doublet lattice method)[25]. The predictions based on Euler's equation, which are taken from Ref. 23 are also plotted for reference.

The agreement between the present calculation (TSP code) and the experimental data is good, especially for the out-of-phase components of both lift and pitching moment for the range of the reduced frequency, $0.1 \leq k \leq 0.3$. The difference between the two (TSP code and the experiment), however, becomes larger as the reduced frequency gets smaller than 0.1. This might be attributed to the effects of the shock wave and turbulent boundary layer interactions, which are neglected in the present potential flow calculations.

The unsteady aerodynamic forces calculated by the present TSP code have been applied to the flutter analysis of a NACA64A010 airfoil (at zero mean angle of attack) in two-degrees-of-freedom (see Fig. 14). The conventional U-g method was employed for determining the flutter boundary.

As an example, the flutter calculations were performed for a binary system (plunging and pitching) having the following parameters:

$$a = -0.30,\ x_{cg} = 0.2,\ r_{cg}^2 = 0.24;$$

$$\omega_h/\omega_\alpha = 0.20$$

where a and x_{cg} are the locations of the elastic axis and the center of gravity, respectively, r_{cg} is the radius of gyration of the airfoil about the c.g. position, and ω_h/ω_α is the uncoupled frequency ratio. These parameters are all non-dimensionalized by the semi-chord b.

The normal modes and the resulting flutter boundary versus Mach number are shown Fig. 15, where μ is the mass ratio and ω_1 and ω_2 are the first and second natural frequencies respectively. For comparison, the flutter boundary, predicted by using the linear aerodynamic theory, (the

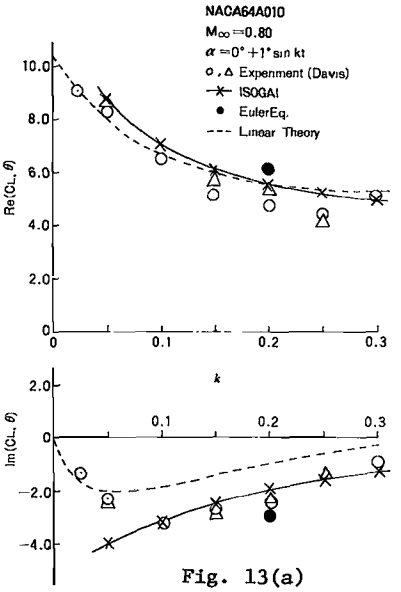

Fig. 13(a)

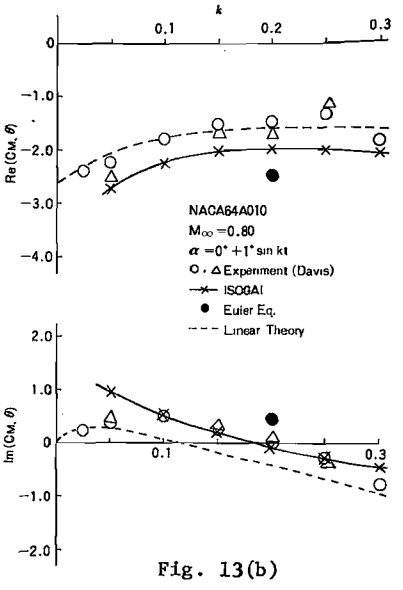

Fig. 13(b)

Fig. 13. Lift and pitching moment versus reduced frequency for NACA64A010 airfoil oscillating in pitch about quarter-chord axis.

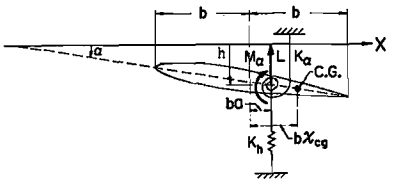

Fig. 14. Binary system of two-dimensional airfoil.

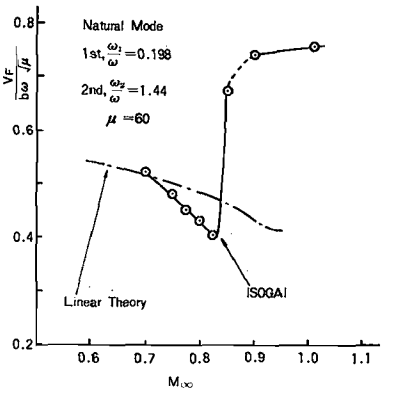

Fig. 15. Flutter velocity coefficient versus Mach number for NACA64A010 airfoil.

doublet lattice method)[25] is also plotted by the dash-dotted line in the same figure. Since it was not possible to obtain the periodic solutions of the aerodynamic forces at Mach number 0.875, the flutter points at M_∞ = 0.85 and M_∞ = 0.90 are connected by the dotted line. The remarkable feature of the behavior of the flutter boundary is that the rapid decrease of the flutter speed toward M_∞ 0.825 and the sharp increase of the speed toward M_∞ = 0.90, thereby producing the "transonic dip". It might be of some value to mention about the shock wave patterns corresponding to this flutter boundary. At M_∞ = 0.825 the shock wave is located about sixty percent of chord position while it reaches to the trailing edge at M_∞ = 0.9. Therefore the effects of the shock wave on the unsteady aerodynamic forces are quite strong at M_∞ = 0.825, while there is no effect of the shock at M_∞ = 0.90. Further details of this flutter analysis and other examples will be published in Ref. (18).

(2) Euler Equation Analysis

Isogai's TSP analysis is efficient in computing. The isentropic shock captured, however, is not accurate when the shock becomes strong. For more accuracy of shock relation, Euler equation analysis should be applied. Ishiguro[26] solved the complete unsteady Euler equations using the time-splitting Lax-Wedroff scheme with artificial viscosity. Magnus and Yoshihara[27], used the similar scheme, without time splitting, before.

In her calculation, the infinite exterior region of physical plane (x, y) is mapped onto the interior of a finite rectangle in the computational plane (ξ η) using three successive mapping transofrmations. The main feature is the use of conformal mapping to get orthogonality in physical plane for the easy treatment of an oscillating airfoil boundary condition. An example for a uniform mesh in the computational plane is shown in Fig. 16 as an image in the physical plane. Here the NLR 7301 airfoil is used with $\Delta\xi$ = 4/100 and $\Delta\eta$ = 1/30. A mesh refinement is made in the vicinity of shock in ξ direction by a factor of 4 as shown.

The mesh system is not altered during the calculation because a quasi-planar boundary condition is assumed.

The two-dimensional unsteady Euler equations are written in the following conservation form:

$$W_t + F_x(W) + G_y(W) = 0 \tag{13}$$

where

$$W \equiv \begin{bmatrix} \rho \\ \rho u \\ \rho v \\ e \end{bmatrix}, \quad F(W) \equiv \begin{bmatrix} \rho u \\ \rho u^2 + p \\ \rho uv \\ u(e+p) \end{bmatrix}, \quad G(W) \equiv \begin{bmatrix} \rho v \\ \rho uv \\ \rho v^2 + p \\ v(e+p) \end{bmatrix},$$

$$p = (\gamma-1)\left\{e - \frac{\rho(u^2+v^2)}{2}\right\}, \quad c = \sqrt{\frac{\gamma p}{\rho}} \tag{14}$$

Here, ρ is the density, u and v are the Cartesian components of the velocity, e is the total energy, p is the pressure, c is the sound speed and γ is the specific heats ratio. Eq. (13) are transformed to the following equations in the computational plane using the chain rule:

$$W_t + F_\xi(W)\xi_x + G_\xi(W)\xi_y + F_\eta(W)\eta_x + G_\eta(W)\eta_y = o \tag{15}$$

where the transormation derivatives are given by the previous mapping procedures.

Using the notation $W_{ij}^N + W(\xi_i, \eta_j, N\Delta t)$, the difference approximation to Eqs. (15) at interior points in the computational rectangle is written as follows:

$$W_{ij}^{N+1} = L_\eta L_\xi W_{ij}^N, \quad W_{ij}^{N+2} = V_\eta V_\xi L_\xi L_\eta W_{ij}^{N+1}.$$

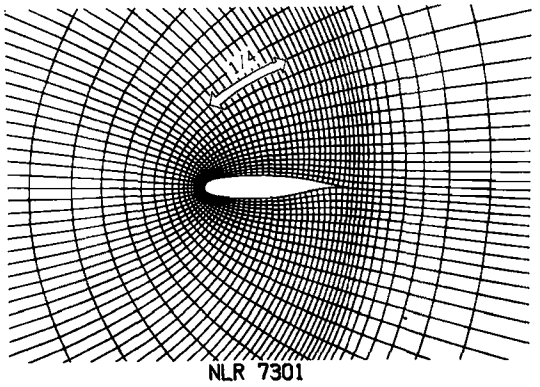

Fig. 16. Image in the physical plane of a uniform mesh in the computational plane.

Here, the integral operators, L_ξ and L_η are the one-dimensional two-step Lax-Wendroff scheme of second-order accuracy. The size of time step is taken as a suitable fraction (less than unity) times ΔT, where ΔT is the maximum time step given by the von Neumann condition. $\Delta t = 0.2\Delta T$ was required to keep stability of the computations. The operators of artificial viscosity V_ξ and V_η are applied and are determined appropriately in the computation so that the computations are stable.

The airfoil boundaty conditions are put along a fixed contour coincident with the airfoil surface location in its median attitude, assuming the amplitude of oscillation is small. In the present calculation, sinusoidally oscillating pitching motion:

$$\alpha(t) = \alpha_0 + \Delta\alpha \sin 2kt,$$

of the airfoil is assumed. Here, α_0 is the mean angle of attack, $\Delta\alpha$ is the pitch amplitude of the angle and k is the reduced frequency given as $k = \omega c/2U_\infty$.

The condition of the sinusoidal rigid body oscillation of the airfoil must be satisfied so that the fluid velocity normal to the surface, matches the body mechanical velocity component in that direction. The dependent variables at the surface are obtained as follows:

$$W_{i1}^{N+1} = 0\ \hat{L}_\eta L_\xi W_{i1}^{N},\quad W_{i1}^{N+2} = 0\ V_\xi L_\xi \hat{L}_\eta W_{i1}^{N+1}, \quad (16)$$

where L_η is an extrapolation operator and 0 is an oscillation operator which performs cumbersome operations after Magnus and Yoshihara. At the upstream boundary, the fixed uniform flow condition was given. On the downstream boundary, simple numerical approximation was made as follows: using the entropy value $s_{IB,j}^{N}$ at the adjacent inner mesh point (IB,j), the boundary values were set equal to the uniform flow values if $s_{IB,j}^{N}$ is nearly s_∞ and continuative condition were set if $s_{IB,j}^{N}$ is greater than s_∞ except pressure which was set equal to p_∞.

Kutta condition is assumed by taking the average of the upper and lower side pressures at the trailing edge.

The procedure of unsteady flow calculation consists of two steps. At first, steady flow solution at uniform stream Mach number M_∞ at mean angle of attack α_0, is calculated as a time asymptotic solution using an appropriate initial condition. Next, the unsteady flow by the pitching motion is started using the above steady flow solution as the initial condition. The computation is continued until a periodicity of unsteady flow is established. It usually takes three to four cycles. The CPU time for one cycle requires about 30 min for k = 0.25 on the NAL AP System. The solutions W at a number of equally spaced phase angles during the pitching cycle are stored in file for Fourier analysis. Forces and moments were calculated from the integration of surface pressure distribution.

Flow past an NLR7301 airfoil was calculated and is shown here[28], in order to compare with the experimental results by Tijdeman[29]. Tijdeman carried out the experiments of steady flow at M = 0.70 and α = 2.5°, 3.0°, and 3.5°.

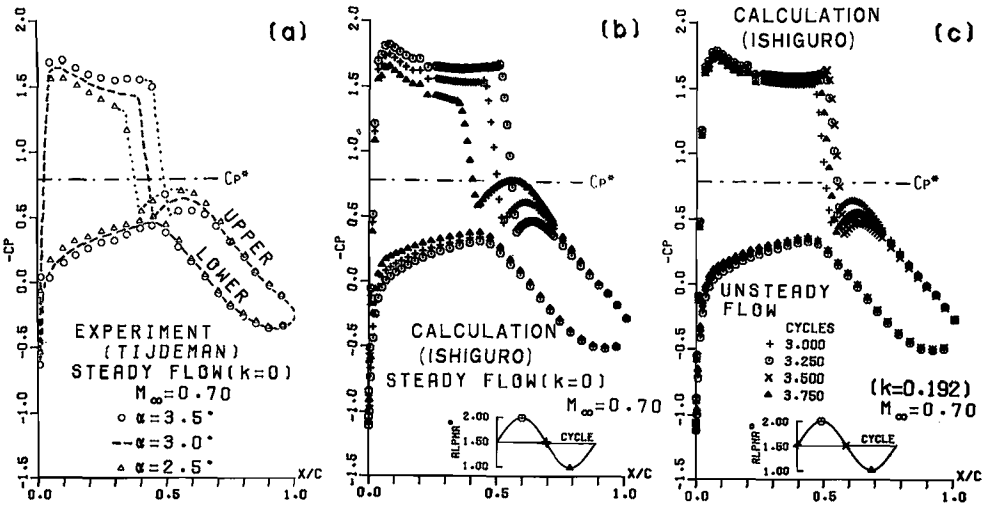

(a) Experiment by Tijdeman, k = 0. (b) Ishiguro, k = 0. (c) Ishiguro, k = 0.192.

Fig. 17. Comparison of pressure distribution.

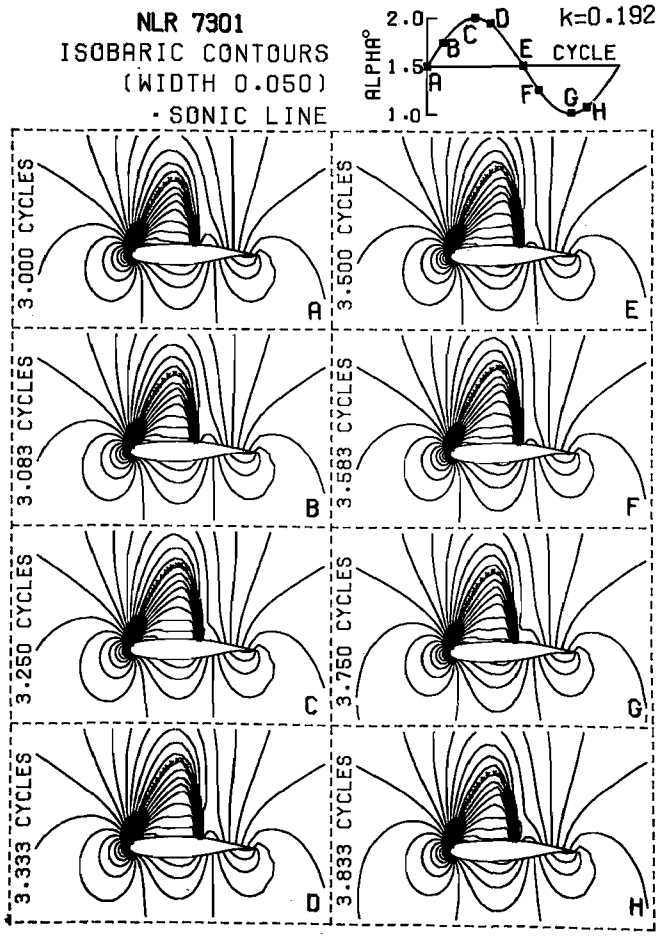

Fig. 18. Isobar patterns and sonic lines at various phase point of the pitching cycle.

Those pressure distributions are shown in Fig. 17 (a). He then carried out the unsteady flow experiment of pitching motion with $\alpha_0 = 3°$, $\Delta\alpha = 0.5°$, and $k = 0.192$ about an axis location ($X_c = 0.4$, $Y_c = -1/60$). Due to the difference of assumption and boundary condition between the present calculation and the experiment, an angle of attack of a steady Euler flow solution closest to his experimental pressure distribution was different from that of the experiment.

Fig. 17(b) shows the result and angle of attack $\alpha = 1.5°$ solution was chose as the best. Then the unsteady flow was computed applying the same pitch amplitude and reduced frequency with α_0 set 1.5°. The resulting instantaneous pressure distribution during the third period is shown in Fig. 17(c). It is noted the amplitude of pressure variation during the pitching motion is smaller than that of a quasi-steady flow condition shown in Fig. 17(b). Fig. 18 shows the isobar pattern and sonic line around the airfoil at various phases of one pitching cycle. The supersonic region continues to grow after the maximum attack angle has been reached and continues to shrink after the minimum angle of attack has been reached.

For a better understanding of flow, Fourier analysis was applied to the local pressure distribution, axial and normal forces and pitching moment. In Fig. 19 the magnitude of local ΔC_p, and its phase of the first harmonic, are compared with those of Tijdeman's result. Thin airfoil theory prediction is also plotted for comparison. The high pressure peaks are generated in the shock wave region. Thin airfoil theory can not predict this phenomena. The present result agrees quite well with the experimental results except for the small deviations for the location of shock and magnitude of components.

3. Three Dimensional Analysis

Takanashi[30] developed a method of analyzing transonic flow around a three dimensional wing based on an integral form of transonic small disburbance equations. The governing integral equation can be written as

$$\Phi(\bar{x},\bar{y},\bar{z}) = \Phi_L(\bar{x},\bar{y},\bar{z}) + \frac{1}{4\pi}\int_{-\infty}^{\infty} d\bar{\xi}\int_{-\infty}^{\infty} d\bar{\eta}\int_{-\infty}^{\infty} \frac{1}{2}\Phi_{\bar{\xi}}^2(\bar{\xi},\bar{\eta},\bar{\zeta})\psi_{\bar{\xi}}(\bar{x},\bar{y},\bar{z},\bar{\xi},\bar{\eta},\bar{\zeta})d\bar{\zeta} \quad (17)$$

where $\bar{\Phi} = k/\beta^2\Phi$, Φ is perturbation potential, $\beta = \sqrt{1-M_\infty^2}$, M_∞ is free stream Mach number, $k = (\gamma+1)M_\infty^2$, $\bar{x} = x$, $\bar{y} = \beta y$, $\bar{z} = \beta z$, Φ_L is a potential of linearized theory,

$$\psi = \frac{1}{\sqrt{(\bar{x}-\bar{\xi})^2 + (\bar{y}-\bar{\eta})^2 + (\bar{z}-\bar{\zeta})^2}} \quad (18)$$

and the domain of integral is the entire flow

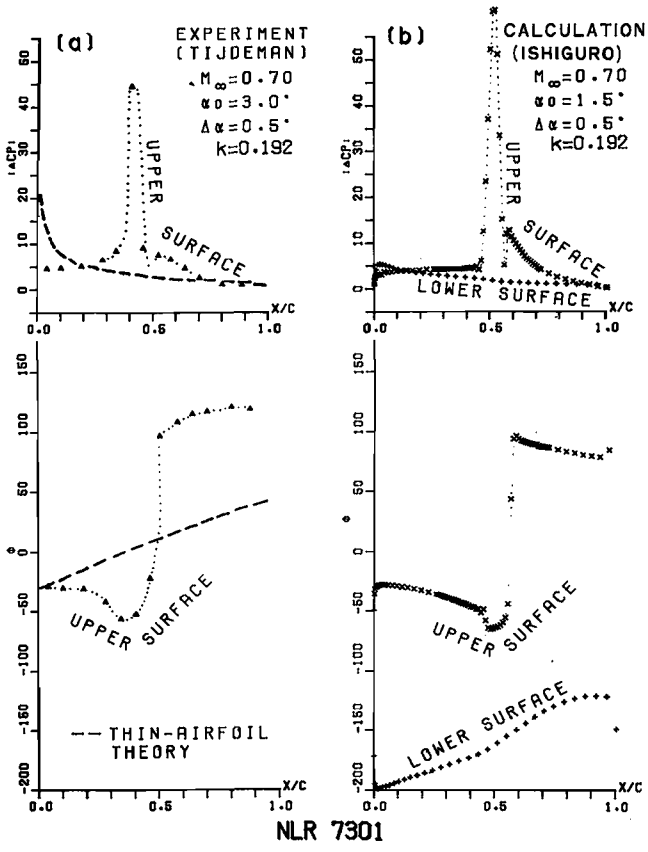

(a) Experiment by Tijdeman. (b) Ishiguro.

Fig. 19. Amplitude and phase lag of the first harmonic of local surface pressure.

field except wing surface, shock wave and the singular point of ψ.

Differentrating Eq. (17) with respect to $\bar{x}$ and putting $\bar{z} = 0$, we obtain

$$\bar{u}(\bar{x},\bar{y},o) = \bar{u}_L(\bar{x},\bar{y},o) + \frac{1}{2}\bar{u}^2(\bar{x},\bar{y},o) - \frac{1}{4\pi}\int_{|\bullet|-\infty}^{\infty} d\bar{\xi}\int_{-\infty}^{\infty} d\bar{\eta}\int_{0}^{\infty} \bar{u}^2(\bar{\xi},\bar{\eta},\bar{\zeta})\psi_{\bar{\xi}\bar{\xi}}d\bar{\zeta} \tag{19}$$

where $\bar{u} = \bar{\Phi}_{\bar{x}}$ and

$$\int_{|\bullet|-\infty}^{\infty}(\ )\,d\bar{\xi} = \lim_{\varepsilon\to 0}\left[\int_{-\infty}^{\bar{x}-\varepsilon}(\ )\,d\bar{\xi} + \int_{\bar{x}+\varepsilon}^{\infty}(\ )\,d\bar{\xi}\right] \tag{20}$$

Evaluation of Eq. (19) requires a knowledge of $\bar{u}(\bar{x},\bar{y},\bar{z})$ over the entire flowfield. Takanashi approximated the variation of $\bar{u}(\bar{x},\bar{y},\bar{z})$ with $\bar{z}$ by the following relations.

$$\bar{u}(\bar{x},\bar{y},\bar{z}) = \bar{u}(\bar{x},\bar{y},0)/[1+2R\bar{z}+\lambda R^2\bar{z}^2] \tag{21}$$

where R and λ are positive real parameters. R and λ are so determined that $\bar{u}_{\bar{z}}$ and $\bar{u}_{\bar{z}\bar{z}}$ of Eq. (21) satisfy the fundamental differential equations at wing surfaces, the ordinate of which is defined by $\bar{f}$:

$$R = -\bar{f}_{\bar{x}\bar{x}}(\bar{x},\bar{y})/[2\bar{u}(\bar{x},\bar{y},0)] \tag{22}$$

$$\lambda = 4 - (\bar{u}^{*2}_{\bar{x}} - \bar{u}^{*}_{\bar{y}\bar{y}})/(2R^2) \tag{23}$$

where the asterisk denotes the value at the sonic point. Substituting Eq. (21) into Eq. (19) we get

$$\bar{u}(\bar{x},\bar{y},0) = u_L(\bar{x},\bar{y},0) + \frac{1}{2}\bar{u}^2(\bar{x},\bar{y},0) + I(\bar{x},\bar{y}) \tag{24}$$

where

$$I(\bar{x},\bar{y}) = -\frac{1}{4\pi}\int_{|\bullet|-\infty}^{\infty} d\bar{\xi}\int_{-\infty}^{\infty} d\bar{\eta}\int_{0}^{\infty}\frac{\bar{u}^2(\bar{\xi},\bar{\eta},0)}{(1+2R\bar{\zeta}+\lambda R^2\bar{\zeta}^2)^2}\psi_{\bar{\xi}\bar{\xi}}d\bar{\zeta}$$

Eq. (21) is different from the approximation used by Spreiter [31], where only $\bar{u}_z$ at the wing surfaces has been considered.

For a rectangular wing, wing surfaces are divided into small rectangles, on which velocity $\bar{u}$ and coefficients R and λ are assumed to be constant (see Fig. 20). Then it is easy to integrate Eq. (24).

Eq. (24) can be written as

$$\bar{u}(\bar{x},\bar{y},0) = 1 \pm \sqrt{1-2(\bar{u}_L+I)} \tag{25}$$

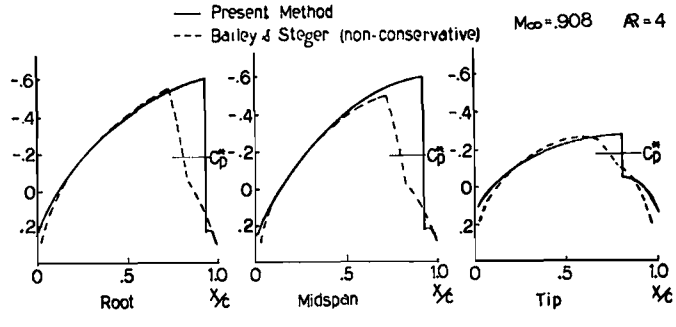

Fig. 22. Pressure distributions on a rectangular wing.

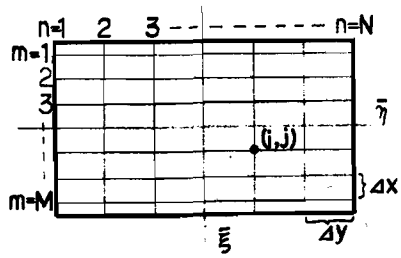

Fig. 20. Computational mesh of a rectangular wing.

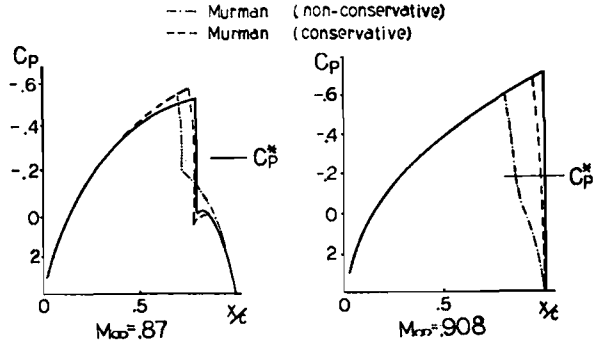

Fig. 21. Pressure distributions on a biconvex airfoil (t/c=0.06).

sign (+) and (-) correspond to supersonic and subsonic flows, respectively. $\bar{u}$ are evaluated by the iteration. In case shock waves exist on the wing surface special attentions are necessary. Assuming the location $\bar{x}_s(\bar{y})$ of shock wave to be somewhere on the wing surfaces. Eqs. (22) and (25) are modified to

$$R = -\mu\bar{f}_{\bar{x}\bar{x}}(\bar{x},\bar{y})/[2\bar{u}(\bar{x},\bar{y},0)] \tag{26}$$

$$\bar{u}(\bar{x},\bar{y},0) = 1 \pm \sqrt{1-2(\mu\bar{u}_L+I)} \tag{27}$$

where $\mu(y)$ is a parameter, which modifies the thickness of the wing temporarily, so that the shock wave locates on $\bar{x}_s(\bar{y})$. μ and the sonic point $\bar{x}^*(y)$ are determined from the condition at which, the value and x derivative of the quantity in the square root of Eq. (27) are zero. If $\mu \neq 1$ after iteration, then the location of shock wave is changed until $\mu = 1$ holds.

Pressure distributions over the 6% circular arc airfoil have been calculated and compared with those of Murman [32] in Fig. 21.

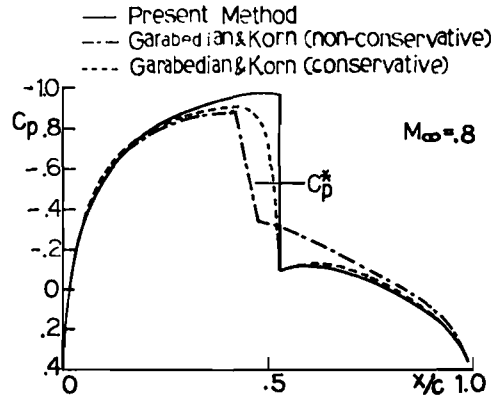

Fig. 23. Pressure distributions on NACA0012 airfoil.

The present calculations agree well with those of Murman based on a conservative scheme. Results on a rectangular wing having the aspect ratio of 4 are shown in Fig. 22 and are compared with the calculations of Bailey & Steger[33], based on a non-conservative scheme. The difference in the location of the shock wave is similar to that between the present results and Murman's non-conservarive calculations. Finally, the result for the round nosed NACA0012 airfoil, calculated by use of Riegel's factor, is compared with the calculation of Bauer et al in Fig. 23. Agreement between the present calculation and the calculation based on a quasi-conservative scheme is good.

4. Viscous Effect Evaluation

The two dimensional analysis and design codes, mentioned above in III(2), incorporate the viscous effect, adding or subtracting the displacement thickness of the turbulent boundary layer to or from the thickness of the airfoil. For three-dimensional flow analysis, however, no viscous effects are incorporated at present. A new finite difference scheme, for three-dimensional compressible turbulent boundary layer equations, is currently being developed by Matsuno[34]. The details are left for Reference (34). His scheme is efficiently fitted for vector processing and has no dependency on the cross-flow direction which is inherent to the well-known Cebeci-Keller's method[35]. The work is progressing presently to accomodate the method to a general plan form of a swept wing and will be presented soon in a separate paper.

When the viscous effects become significant, the above described modification, using the boundary layer equations, is not adequate and the more accurate approximation of Navier-Stokes equations must be applied. Analysis at such a flow condition, at a high transonic Mach number with a strong shock wave boundary layer interaction, is inevitable during the process of transonic wing design. For this purpose, the development of two-dimensional time-averaged Navier-Stokes analysis codes is now under study at NAL.

It is still in the preliminary stage and is too early for presentation. Only a brief outline will be given here. One is an explicit finite difference scheme. The disadvantage of such a method is the well-known short time step for stability. Thus is requires a large amount of computing time. Nevertheless, such a method is more reliable than recently developed time-efficient inplicit schemes because of its simplicity and long-time experiences. Consideration for the extensions of the method to multi-element airfoil and three-dimensional wing are also being taken into account. Grid generation methods are also studies to apply for this purpose. Another scheme under development is the implicit scheme using the approximate factorization technique [36]. The original scheme, though being time-efficient, is not satisfactory in the practical calculations due to deteriorating interference between the scheme and grid geometry, conservation characteristics, and stability. Therefore, improvements are being undertaken for better boundary condition, mesh geometry and numerical algorithm. The result obtained so far is acceptable. These Navier-Stokes code developments are expected for practical application on the planned forthcoming computer called Numerical Simulator; the details of which are given later in the present paper.

IV. Application of Computational Aerodynamics

1. Optimization of Airfoils

Hicks[37] introduced the numerical optimization method incorporating non-linear programming with the aerodynamic analysis code. His method is epoch making in the sense that an optimum airfoil can be obtained antomatically and that the conditions at off design point, no drag creep for example, can be incorporated. At the present time it is a restriction, as well as a progression, that, in his method, the optimization was conducted through parametric change of airfoil geometry without referring to the historican accumulation of knowledge about the optimum pressure distributions. Airfoil geometries of sufficient characteristics can not be represented by a few parameters, whereas to use too many parameters is not practical due to the prohibitive time consumption for computation. Based on the above, satisfactory results have not yet been achieved for designing completely new airfoils, although for the modification of given airfoils good results have been accomplished. For this reason it would be more effective to design airfoils using pressure distributions which have historical accumulations in order to obtain optimum airfoils by use of a few parameters in a short time.

Kamiya designed airfoils having specified pressure distributions represented by several parameters by use of Ishiguro's method described previously in III.1(2). Fig. 24 shows an example of the pressure distributions. The pressure distributions are represented by appropriate curves drawn through two neighboring points of L,A,B,C,D and T for the upper surface and L,E,F, G and T for the lower surface. These pressure distributions are difined after the guide line proposed in Ref. 1. Optimizations are conducted by changing the values of x/c or p/p_o of these points manually, where x is streamwise distance from the leading edge, c is the chord length, p is static pressure on the airfoil surfaces and p_o is the stagnation pressure.

Figs. 25, 26 and 27 show an example of the optimization. The design point for this study is defined to be $M_\infty = 0.74$, $t/c = 0.122$ and $C_L = 0.85$ where t/c is the thickness ratio. The design objective is wave drag minimization at

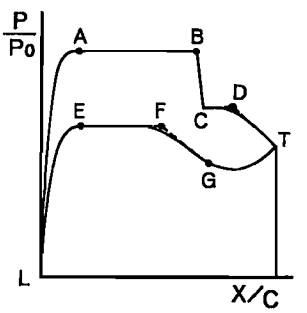

Fig. 24. Conceptional diagram of a specified pressure distribution.

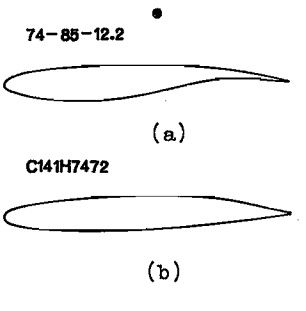

Fig. 25. Examples of optimized airfoil geometry.

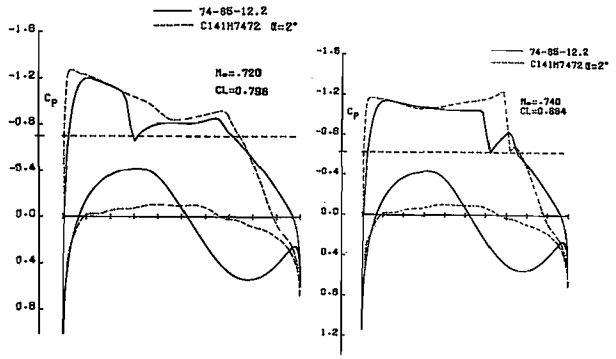

Fig. 26 (a). Fig. 26 (b).

Fig. 26. Pressure distributions on the airfoils shown in Fig. 25.

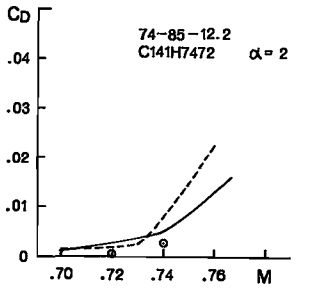

Fig.27. Calculated inviscid drag coefficient.

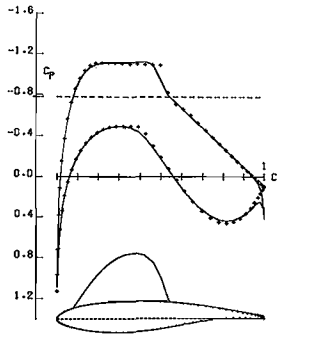

Fig. 28. Example of optimized airfoil geometry.

the design point under the constraint condition that the location of the shock wave on the upper surface be at 70% of chord from the leading edge and that the flow be inviscid. The resulting airfoil is referred to as 74-85-12.2 according to the values of M_∞, C_L and t/c at the design point. Fig. 25 (a) shows the geometry of 74-85-12.2 and Fig. 25(b) shows that of the airfoil referred to as C141H7472 in Ref. 38, the design objective of which is also the inviscid drag minimization at the design point having $M_\infty = 0.72$ and $\alpha = 2.0°$, through changing the geometry of the upper surface without changing the thickness-to-chord ratio under the constraints conditions of:

$C_n > 0.85$ and $C_d < 0.002$ at $\alpha = 2°$ and $M_\infty = 0.74$. The thickness-to-chord ration of both airfoils are the same.

The dotted lines of Fig. 26(a) and (b) show pressure distributions of C141H7472 at $\alpha = 2°$ for $M_\infty = 0.72$ and $M_\infty = 0.74$ respectively, calculated at NAL which coincide exactly with those described in Ref. 38. The solid lines show pressure distributions of 74-85-12-2 at the same M_∞ and CL as those of C141H7472. The strength of the shock waves at $M_\infty = 0.74$, for example, are weaker for 74-85-12.2 than for C141H7472. Therefore the drag coefficient of the former is smaller than that of the latter except in a region near $M_\infty = 0.72$ where the difference is small as shown in Fig. 27. Where the drag coefficient of the latter calculated at NAL is somewhat different from that described in Ref. 38 contrary to the excellent coincidence of the pressure distributions. The reason for which is not clear Figs. 26 and 27 suggest that it is easy to optimize airfoils by changing pressure distributions parametrically rather than by changing airfoil geometry so that one can obtain good airfoils in a short time if one applies the numerical optimization scheme to pressure distributions specified parametrically.

Fig. 28 shows an example of airfoil designs for which C_L/C_D is maximized for the conditions: $M_\infty = 0.7$, $t/c = 0.15$, $R_e = 2 \times 10^7$ and $H_{max} \leq 2.25$, where R_e is the Reynolds number and H_{max} is the maximum value of the ratio of momentum thickness to displacement thickness of the boundary layer on airfoil surfaces. The condition on H_{max} is assigned in order to avoid boundary layer separation. The value of C_L/C_D in this case is 88.0.

2. Evaluation of an Airfoil Analysis Code

As an example of the evaluation of analysis codes, the evaluation of the airfoil analysis code of Bauer et al[16] is described here. Calculations usually diverge at a free stream Mach number, higher than some critical value, which changes depending upon airfoil geometry and lift coefficient. Fig. 29 shows an example of such a boundary. The calculations diverge in the hatched region for the airfoil described in Ref. 1 at the value of a Reynolds number of 2×10^6.

Fig. 29 also shows the locus of a drag divergence Mach number. In Fig. 30 the calculated pressure distributions are compared with those for experiment at the same M_∞ and C_L where the solid lines denote the calculations based a non-conservative scheme (NC) and the dotted lines denote those based on a quasi-conservative scheme (QC). In both cases the relaxation procedure is modified to be suitable for the NAL AP system (AP). Fig. 30(a) shows the pressure distributions at the free stream Mach number appreciably lower than M_{DD}.

Fig. 30(b) shows those at M_{DD} and Fig. 30(c) shows those at M_∞ appreciably higher than M_{DD}. The non-conservative calculations agree well with the experimental data whereas the quasi-conservative calculations do not agree with the experiment if M_∞ is higher than M_{DD} where the shock wave is strong.

As to the value of M_{DD} the quasi-conservative calculations agree with the experiment better than the non-conservative calculations[39]. In Fig. 31 the quasi-conservative calculations are compared with the experiment for thirteen airfoils described in Refs. 1 and 2. The calculated values of M_{DD} are always lower than the experimental ones. The averaged discrepancy is about 0.02.

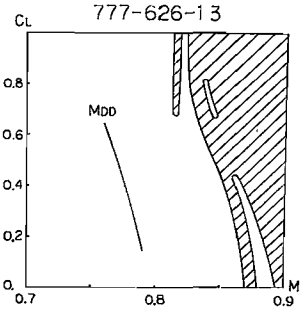

Fig. 29. Region of convergence for analysis of an airfoil and M_{DD}-C_L curve.

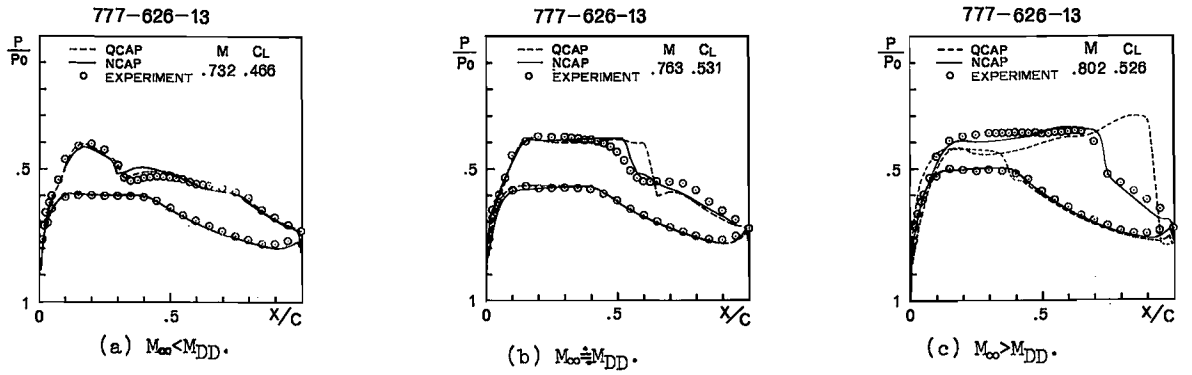

(a) $M_\infty < M_{DD}$. (b) $M_\infty \fallingdotseq M_{DD}$. (c) $M_\infty > M_{DD}$.

Fig. 30. Pressure distributions of 777-626-13 airfoil.

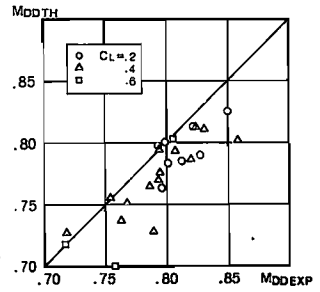

Fig. 31. Comparison between experimental and computational drag divergence Mach number.

Table 1. Main characteristics of NAL two-dimensional transonic wind tunnel.

NAL Two-Dimensional Transonic Wind Tunnel	
Type	Intermittent blowdown
Mach number range:	0.2 - 1.15
Maximum Reynolds number:	40 x 10^6 (refered to the model chord length of 0.25m, and at M=0.8)
Test section size:	0.3m x 1.0m cross section, and 3.0m in streamwise length
Stagnation pressure:	392 to 1176kPa
Running time:	9-100 sec.
Turn around time:	Less than 40 min.

V. Facilities

1. High Reynods Number Two-Dimensional Wind Tunnel

The need for high Reynolds number tests at transonic speeds has been recognized since the late sixties. As a first step towards high Reynolds number testing, construction of a two-dimensional pressure wind tunnel[5], including all the back up facilities and the data processing system, was commenced in 1973, and finished in March 1980.

The general view is shown in Fig. 32. Main characteristics are shown in Table 1 and the capability of this wind tunnel is shown in Fig. 33.

Models are mounted so as to span completely the 0.3m width of the test section and are supported at each end by clamps which are mounted just outside of the side wall. Air leakage at the side walls is prevented by O-rings.

The top and bottom walls of the test section are made up of slotted walls of variable open area ratios of 0-10%. The side walls are equipped with a pair of boundary layer suction plates of 0.465m in effective diameter, 0.01m thick, made of 5μ-sintered metal; flow resistance through

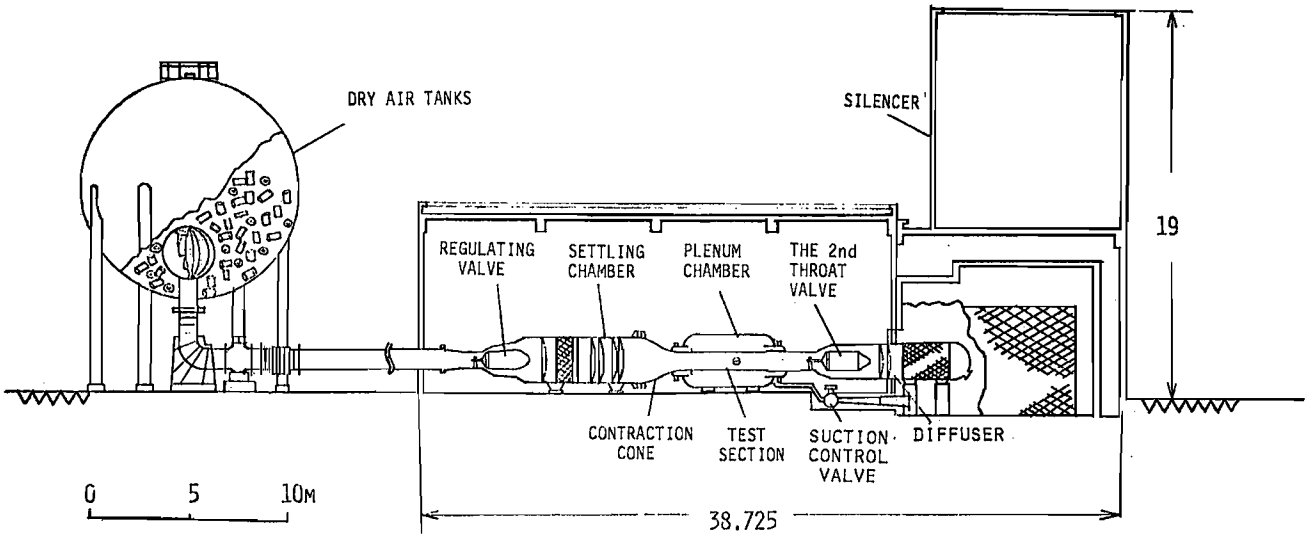

Fig. 32. NAL two-dimensional transonic wind tunnel.

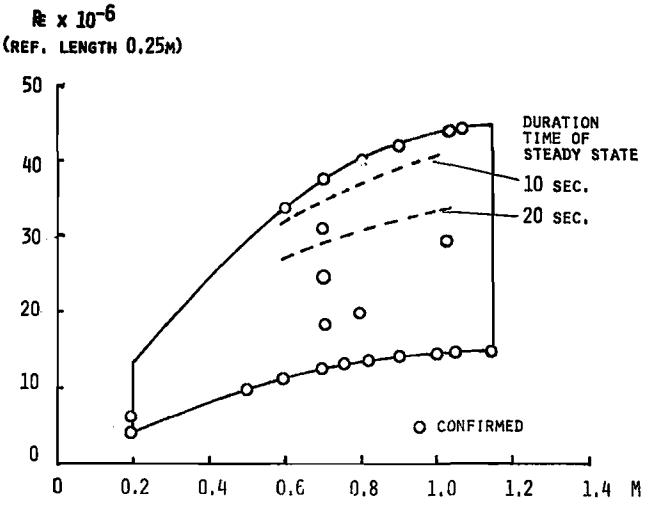

Fig. 33. Capability of NAL two-dimensional wind tunnel.

these plates is 60,000 x dynamic pressure. If optical observation such as shlieren photographs or laser holography should be required, these suction plates can be replaced by glass windows. Pitot rake for wake traversing is inserted into the flow through the slit opened in a side wall.

Data processing is taken with 48 channels of an AD converter, an HP-21-MXE series CPU with memories of 96kW, a Versatec 1,200 A plotter, a line printer, magnetic disks, a magnetic tape recorder and so forth.

2. The Numerical Simulator Project

At the NAL the FACOM 230-75 dual CPU system was installed in 1975 and one of the CPU's was replaced by an APU[40] (array processor unit) in 1977. The APU uses high speed IC devices and consists of three pipelines: addition, multiplication and logic operations. The maximum hardware speed is 22 MFLOPS for adding, 11 MFLOPS for multiplying and 22MFLOPS for a vector inner product. Vector dividing is the weakest point of the pipeline and the speed is 1.2 MFLOPS.

Table 2 shows the ratio of CPU time to APU time for several kinds of computations. An average value of five was accomplished. This performance is better than the CDC7600.

The performance of the AP System has not yet surpassed by the latest general purpose computer. But within a few years the machine becomes obsolete. It has several weak points. The memory is limited to 1 million words of which one job can occupy only less than half. It is not large and high speed enough to run Navier-Stokes code. Three dimensional codes, now available, are only the transonic potential codes.

A new vector processor system is under study at NAL to overcome those shortcomings and to meet the demand of large scale computations. The system under study is provisionally called Numerical Simulator. A Working Group for technical evaluation of the NS Project has been working since last year. It covers evaluation of the necessity, technical possibility, required performances and specifications of the system, and applicable fields of interest. This is similar to the NASF project of NASA[41].

Table 2. Speed Ratio of AP Application Programs to CPU.

Method of Calculation	APU (sec)	CPU (sec)	RATIO (CPU/APU)
1. Eigenvalue QL Method	468.4	3,870.0	8.3
2. Quadruple Integral	516.0	3,000.2	5.8
3. PDE by FDM	123.0	670.6	5.5
4. GAUSS-SEIDEL Iteration Method	47.2	210.5	4.5
5. PDE by FDM	1,132.9	6,527.1	5.8
6. Matrix Inversion (Dimension: 400 x 400)	15.6	108.7	7.0
7. Eigenvalue Iteration Method (Dimension: 700 x 700)	1.0	21.3	21.3

Table 3. Computer Requirement for Three-Dimensional Flow Analysis.

Code*	TFP	TANS
Variables	12	
Grid Points	10^6	2×10^6
Memory	10^7	10^8
Operations/point	10^2	10^3
Iterations	10^3	10^3
Performance**	200	3000

* TFP: Transonic Full Potential code

TANS: Time-Averaged Navier-Stokes code

** MFLOPS

Table 3 shows a crude estimation of computer requirements for 3-dimensional transonic flow analysis. It should be noted that even the transonic full potential (TFP) calculation requires a speed of 200 MFLOPS and a memory of 10 million words when the production code of a wing-body configuration should be run on a practical design pace. A time-averaged Navier-Stokes (TANS) calculation needs a computer with a one-order higher speed, if similar productivity, as the former, is vital. At present, the required performance of a Numerical Simulator is a speed of 800 to 1,000 MFLOPS and a main memory of 128 million words (Fig. 34.)

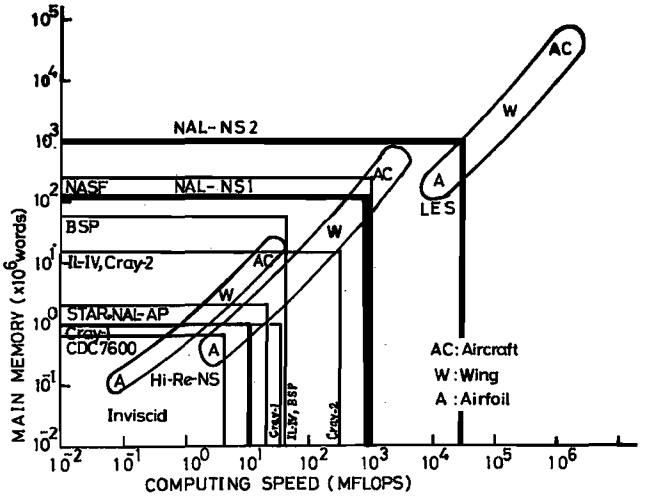

Fig. 34. Performance of several computers.

Several design models are studied. Design A is a multiple pipeline processor system made of several Pipeline Processing Elements (PE's). Each PE itself is a gigantic processor with several pipelines and several ten million words of PE Memory performing several hundred MFLOPS of speed. The total performance is multiplied by the number of PE's. Design B is a multiple processor system made of one hundred Processing Elements. A common main memory and the PE's are connected through a Matrix Switch. Each PE has a speed of 20 to 30 MFLOPS, comparable to the present AP system. Design C is a distributed array processor system of two-dimensions.

We except the Numerical Simulator is not the last computer and its successor should be built before 1990. Therefore, the architecture should be one which can be extended to Numerical Simulator 2 without basic modification of design. The NS2 will have a speed of 30 billion FLOPS and a memory of 1 billion words under the same design and using the most advanced elementary devices of the day. Commercial vector processors for general purposes will not meet our requirement. We think, from our experience, this type of computer should be order-made. It is not amazing that the estimated cost is less than 10 billion yen because ready-made hardware technology will be fully utilized. If such a budgetary measure is taken, the Numerical Simulator is expected to be operational before the mid 80's.

References

1. Kamiya, N. et al, AIAA Paper 78-1221, 1978.
2. Kamiya, N., NAL TR-299, 1973.
3. Jones, J.L., NASA CP-2009 1976.
4. Staff of NAE, LTR-HA-4, 1970.
5. Endo, H., J. Japan Soc. Aero. Space Sci., Vol.26, No.299, pp611-617, 1978.
6. Nicks, O.W., NASA CP-2009, 1976.
7. Shigemi, T., NAL TR to be published.
8. Nieuwland, G.Y., NLR-TR-T 72, 1967.
9. Takanashi, S., Trans. Japan Soc. Aero. Space Sci., Vol.17, No.34, pp246-263, 1973.
10. Nakamura, M., Preprint of the 7th Annual Meeting of Japan Soc. Aero. Space Sci., 1976.
11. Nakamura, M., J. Japan Soc. Aero. Space Sci., Vol.26, No.291, pp191-198, 1978.
12. Nakamura, M., NAL TR, to be published.
13. Sobieczky, H. et al., AIAA Paper 78-1114, 1978.
14. Ishiguro, T., NAL TR, to be published.
15. Tranen, T.L., AIAA Paper No.74-501, (1974).
16. Bauer, F., Garabedian, P. and Korn, D., Supercritical Wing Sections III, Springer Ver., (1977).
17. Bauer, F., Garabedian, P., Korn, D. and Jameson, A., Supercritical Wing Sections II, Springer Ver., (1975).
18. Isogai, K., NAL-TR, to be published.
19. Ballhaus, W.F., and Goorjian, P.M., AIAA Journal Vol.15, No.12, Dec. 1979, pp1728-1735.
20. Jameson, A., Second AIAA Conference on Computational Fluid Dynamics, Hartford, Connecticut, June 1975.
21. Bauer, F., and Korn, D., Second AIAA Conference on Computational Fluid Dynamics, Hartford, Connecticut, June 1975.
22. Isogai, K., AIAA Paper 77-448, 1977.
23. Davis, S.S., and Malcolm, G.N., AIAA Paper 79-0769, 1979.
24. Davies, J.A. and Petrie, S.L., AIAA Paper 79-0330, 1979.
25. Albano, E. and Rodden, W.P., AIAA Journal, Vol.7, Feb. 1969, pp.279-285
26. Ishiguro, T., Theoretical and Applied Mechanics, Vol.28, pp.421-432, 1980.
27. Magnus, R. and Yoshihara, H., AIAA J., Vol.13, 1622, 1975.
28. Ishiguro, T., NAL TR - to be published.
29. Tijdeman, H., NLR TR 77090 U, 1977.
30. Takanashi, S., Preprint of 11th Fluid-dynamics Conference, Japan Soc. Aero Space Sci. pp.86-89, 1979.
31. Spreiter, J.R. and Alksne, NACA Rept. 1217 (1955)
32. Murman, E.M., AIAA J. Vol.12, No.5, pp.626-633, 1974.
33. Bailey, F.R. and Steger, J.L., AIAA Paper 72-189, 1972.
34. Matsuno, K., Preprint of the 17th Symporium on Aircraft, Jap. Soc. Aero. & Space Sci., Nov., 1979.
35. Cebeci, T., Kaups, K. & Ramsey, J.A., NASA CR-2777, (1977)
36. Steger, J.L., AIAA Paper No.77-665, (1977).
37. Hicks, R.M. and Vanderplaats, G.N., SAE Paper No.770440, 1977.
38. Lores, M.E., Burdges, K.P. and Shrewsbury, G.D., NASA CR-3065, 1978.
39. Kawai, N. et al., NAL TM-357, 1978.
40. Miwa, O. et al., Fujitsu, Vol.29, No.1, pp.93-128, 1978.
41. Chapman, D.R., AIAA Journal Vol.17, No.12, pp.1293-1313, 1979.